

# A planar electromagnetic energy harvesting transducer using a multi-pole magnetic plate

Shad Roundy<sup>a,\*</sup>, Eri Takahashi<sup>b</sup>

<sup>a</sup> University of Utah, 50 S. Central Campus Drive, Salt Lake City, UT 84112, USA

<sup>b</sup> EcoHarvester Inc., 46 Shattuck Square, Suite 10, Berkeley, CA 94704, USA

## ARTICLE INFO

### Article history:

Received 29 October 2012

Received in revised form 6 March 2013

Accepted 15 March 2013

Available online xxx

### Keywords:

Energy harvesting

Electromagnetic

Planar transducer

## ABSTRACT

We report on the development of a new planar electromagnetic energy harvesting transducer. The transducer can be realized with low cost printed circuit board technology and leverages recent advancements in the manufacture of multi-pole magnetic sheets. We develop a detailed analytical model to predict the performance of the transducer and to guide the design process. Several specific features of the model, such as voltage dependence on coil routing, are validated experimentally. The basic transducer can be used for energy harvesting devices using a linear vibration or direct force input. We demonstrate the technology with prototypes that use a direct force input that displaces the proof mass and then releases it, allowing it to freely oscillate. The device performance closely matches simulation and results in 1.1 mJ of generated energy and an efficiency of 9%. The model indicates that fairly simple improvements can push the efficiency up to 20%.

© 2013 Elsevier B.V. All rights reserved.

## 1. Introduction

Researchers have studied harvesting energy from vibrations and motion resulting from direct force inputs for well over a decade [1–4]. Vibrations, inertial motion, and direct force inputs provide energy for many wireless sensor and low power communication devices [5,6]. Several companies have been founded based around vibration or motion based energy harvesting [7–9]. However, most of the prototypes and products developed rely on solutions that are not in a planar form factor and are expensive to implement. For example, while piezoelectric sheets or bimorphs are thin, the motion required to generate energy is typically out-of-plane motion [10,11]. Electromagnetic generators often require magnets, coils, or proof masses that work best in a form factor that ends up looking like a cube or fat cylinder [12,13]. One exception is the work by Zhu et al. [14] in which a planar Halbach array is assembled to implement a planar generator. The goal of the work presented in this paper is to present a thin, planar energy harvesting transducer implemented with a novel multi-pole magnetic sheet. The device presented here can be implemented with a single magnetic element thus reducing assembly costs compared to an architecture requiring the assembly of multiple magnets. Furthermore, the

planar coils are implemented in a standard low cost printed circuit board (PCB) process.

The academic and research literature is rich with electromagnetic motion based energy harvesters [15–17]. Several multi-pole magnetic generators have been reported [18–20]. These include both rotational generators [19,20] and linear generators [21]. The work presented here differs in at least two aspects: (1) it makes use of new manufacturing techniques enabling fine pitch multi-polar magnetic sheets [22], and (2) it uses a unique coil configuration to achieve a high generated voltage (greater than 3 V) from linear oscillatory motion in a very thin form factor. Furthermore, we present an analytical model that accounts for practical considerations with coil geometry and position when implemented in standard printed circuit board (PCB) technology.

Section 2 presents the basic operating principle of the transducer. In Section 3 we derive a detailed analytical model of this planar generator and explore some of the practical considerations in predicting the power generated. Section 4 contains experimental results. In Section 5 we discuss some of the strengths and limitations of the devices built. We also discuss opportunities for improvement and the magnitude of expected improvements.

## 2. Operating principle

Fig. 1 shows an illustration of the basic device concept. The device consists of a printed circuit board (PCB) with planar coils, a multi-pole magnetic sheet, and springs which suspend the magnet over the PCB and maintain the gap between them. The flexures are

\* Corresponding author. Tel.: +1 801 581 4304; fax: +1 801 585 9826.

E-mail addresses: [shad.roundy@utah.edu](mailto:shad.roundy@utah.edu) (S. Roundy), [eritaka@ecoharvester.com](mailto:eritaka@ecoharvester.com) (E. Takahashi).

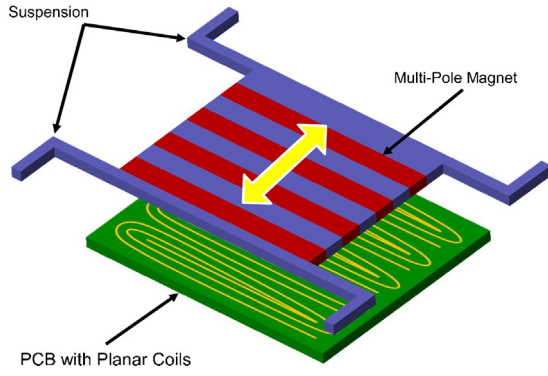


**Fig. 1.** Schematic of basic transducer concept. A multi-pole magnet is suspended over the PCB with planar coils. As the magnet moves over the top of the PCB, voltage is generated in the planar coils.

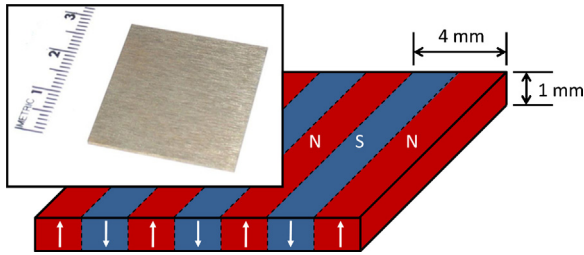


**Fig. 2.** Illustration and image of the multi-pole plate magnet used for this work. Illustration shows magnet dimensions. Inset image shows the actual magnet plate used in the tested prototypes.

designed to constrain the motion to the direction indicated in Fig. 1. The suspended mass can be driven either by vibrations, inertial movements, or a direct force input.

The illustration in Fig. 2 shows a 1 mm thick magnetic sheet with a pitch of 4 mm. The lateral dimensions of the magnetic sheet are 28 mm × 30 mm. The illustration indicates the poling of the magnet, and the inset image shows the magnet itself. It is a NdFeB magnet manufactured for this application by Intermetallics Co. Ltd [22] using a proprietary process. The magnets used for this study have thickness and pitch dimensions as shown in Fig. 2, however, the pitch dimensions can be reduced if desired for the application.

The magnet can be suspended above planar coils as illustrated in Fig. 1. In our case, the coils are implemented in a multi-layer PCB. The basic geometry of the coil is illustrated in Fig. 3. This configuration easily allows for multiple coils to be wired in series on each layer of the circuit board, and each layer to be wired in series with other layers resulting in a high voltage output. No special PCB fabrication technology is needed, and standard but expensive options such as blind vias are not required. The prototype for which results

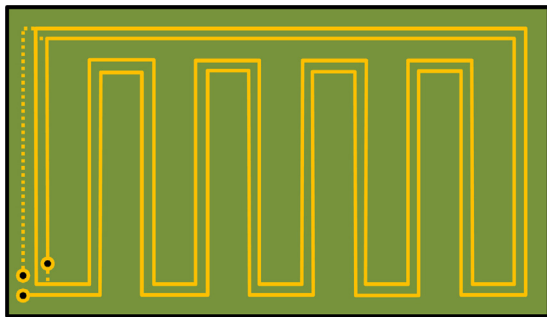


**Fig. 3.** Illustration of planar coils on PCB. Two series coils shown. Dotted lines indicate metal traces on the back of the PCB in a different location than the front layer traces.

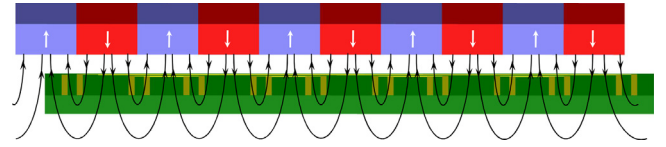


**Fig. 4.** Illustration of the magnetic flux captured by the planar coils on the PCB. Note that the direction of the magnetic flux captured by each rectangular coil is the same.

are presented has 5 coils in series in each of 6 layers of the PCB. Fig. 4 illustrates how the coils capture the magnetic flux emanating from the multi-pole magnet. The magnetic flux captured by each coil is in the same direction. Therefore, the voltage produced by each coil is exactly in phase and adds together as long as the coil pitch matches the magnet pitch.

Fig. 5 shows an alternate coil configuration. The direction of the current flow is shown by the arrows. The coils are wired in a series configuration such that the voltage from each adjacent coil adds together. This coil configuration is slightly more space efficient on a single layer and therefore in principle could result in better power transduction. However, in practice it does not result in more power output (see Sections 4 and 5).

### 3. Theory

We developed an analytical simulation model based on electromagnetic theory. Eqs. (1) through (3) describe the coupled electro-mechanics of the system.

$$\frac{di}{dt} = -\frac{R + R_c}{L}i + \frac{1}{L}V_s \quad (1)$$

$$V_s = -\frac{d\Phi}{dt} = -N \frac{d}{dt} \left( \int \int \mathbf{B} \cdot d\mathbf{A} \right) \quad (2)$$

$$m\ddot{x} + b\dot{x} + N(\mathbf{i} \times \mathbf{B}) + kx = F_{in} \quad (3)$$

where  $i$  is the current through the coils;  $R_c$  the coil resistance;  $R$  the load resistance;  $L$  the coil inductance;  $V_s$  the generated open circuit voltage;  $\Phi$  the magnetic flux captured by coils;  $N$  the number of coils;  $\mathbf{i}$  the vector along the length of the coil;  $\mathbf{B}$  the magnetic flux density;  $d\mathbf{A}$  the element of surface circumscribed by the coil;  $x$  the position of the magnet with respect to the PCB;  $m$  the mass of the magnet;  $b$  the mechanical damping coefficient;  $k$  the stiffness of the flexures; and  $F_{in}$  the input force to the magnet.

The voltage generated is defined by the change in total magnetic flux captured by the coils (Eq. (2)). The flux is determined by the surface integral of the dot product of the flux density vector  $\mathbf{B}$ , and the vector normal to the surface enclosed by the coil  $\mathbf{A}$ . The system is constrained such that the  $\mathbf{A}$  vector (and thus each element  $d\mathbf{A}$ ) is normal to the surface of the PCB, which we define as the  $y$

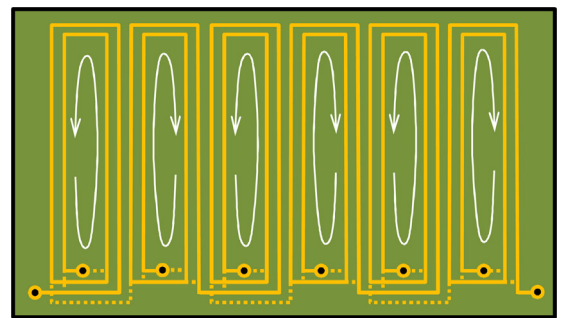


**Fig. 5.** Alternate coil configuration. Two series coils shown for a two layer PCB. Coils are repeated on back side of PCB. Dotted lines indicate metal traces on the back of the PCB in a different location than the front layer traces. This alternate configuration is slightly more space efficient, but interconnection between coils is more complex.

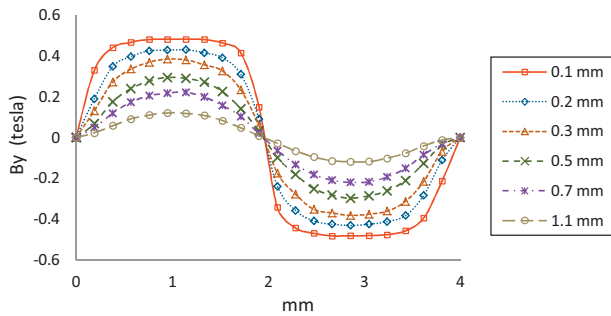


**Fig. 6.** Finite element simulation results. Magnetic flux density perpendicular to the magnet at various distances shown for one pair of magnetic poles (1 pitch).

direction. Therefore, only the  $y$  component of the  $\mathbf{B}$  vector is important in determining the flux captured by the coil. Using this geometric constraint, Eq. (2) can be simplified as shown in Eq. (4). Similarly, Eq. (3) can be re-written as shown in Eq. (5).

$$V_s = -\frac{d\Phi}{dt} = -NI \frac{d}{dt} \left( \int_{x_1'}^{x_2'} B_y(x') dx' \right) \quad (4)$$

$$m\ddot{x} + b\dot{x} + NIB_y i + kx = F_{in} \quad (5)$$

where  $x'$  is the linear position along the PCB;  $B_y$  the  $y$  component of the magnetic flux density vector; and  $l$  the length of one side of the rectangular coil.

### 3.1. Analytical description of magnetic flux density

The solution to Eqs. (1), (4) and (5) is straightforward if each coil captures the same amount of magnetic flux. However, in our case each coil on a given layer of the PCB is in a slightly different lateral position. So, the voltage generated by one coil will have a different magnitude than the voltage generated by the adjacent coil. Additionally, the coils on layers closer to the magnet surface will generate more voltage than those further away as the magnetic flux is stronger closer to the magnet surface. If we were to assume that each coil is in the same lateral position, or that each layer is equally productive, our estimates would contain significant errors. One solution is to use finite element models to calculate the voltage generated by each individual coil. This, however, is cumbersome as a design tool, and does not provide much intuitive insight. Therefore we developed an analytical description of the magnetic flux density perpendicular to the PCB ( $B_y$ ) as a function of the lateral position and the distance from the magnet surface. We used finite element simulations to validate our analytical description. The analytical solution is then used during the design process to understand tradeoffs and optimize the design.

Fig. 6 shows a graph of the simulated magnetic flux density ( $B_y$ ) as a function of lateral position ( $x'$ ) at various distances from the magnet. Looking at Fig. 6, we can approximate the shape of the  $B_y(x')$  curve with a sinusoid as long as the coils are at least 0.2 mm away from the surface. Even in cases where the coil is slightly closer, the sinusoidal assumption results in negligible errors. The magnitude of the  $B_y(x')$  curve gets smaller further away from the magnet as expected. We fitted the magnitude of the  $B_y(x')$  curve with an exponential function. Measurements taken with a gaussmeter at various distances from the center of the magnet validate the simulated magnitude of the flux density curves. Fig. 7 shows measured and simulated values for the magnitude of the flux density curves. Note that the pitch of the multi-pole magnet is 4 mm, so each magnetic pole is 2 mm in width. The sensing element in the gaussmeter used is 1 mm in width, so it effectively averages over a 1 mm wide section of the curve. Assuming a sinusoidal curve, this

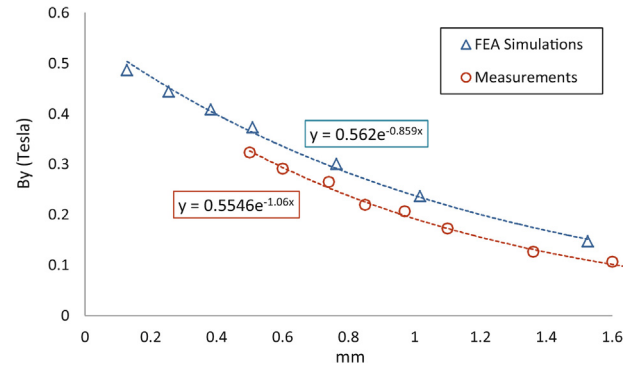


**Fig. 7.** Simulated and measured magnitude of the flux density curve versus distance from the magnet. Exponential fitted equations for both sets of data are also shown. The fitted equation from the measured data was used for the simulation model.

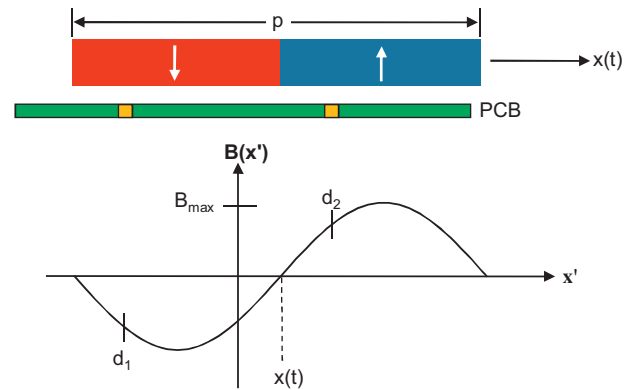


**Fig. 8.** Magnetic flux density approximation and definition of variables.

averaging effect can be factored out, which has been done for the data shown in Fig. 7. The experimental data is offset just below the simulated curve. However, an exponential fit works well in both cases. We used the fitted equation from the experimental data in the model. Combining the sinusoidal model for  $B_y(x')$  with the exponential curve fit results in the expression in Eq. (6) for the magnetic flux density as a function of lateral position and distance from the magnet surface.

$$B_y(x') = B_{\max} e^{-\alpha y(i)} \sin \left( \frac{2\pi}{p} (x' - x(t)) \right) \quad (6)$$

where  $B_{\max}$  is the maximum value of magnetic flux density at the magnet surface extrapolated from Fig. 7;  $y(i)$  the distance from the magnet surface of the  $i$ th layer of the PCB; and  $p$  the magnet pitch.

Using Eq. (6), a closed form expression for the magnetic flux ( $\Phi$ ) captured by each coil can be developed. However, we first need to make explicit the definition of the position variables  $x'$  and  $x(t)$ . Fig. 8 shows two poles of the magnet, a cross section of the PCB, and the assumed shape of  $B_y(x')$ .  $x'$  is the position along the PCB.  $d_1$  and  $d_2$  mark the positions of the metal lines of a single rectangular coil on the  $B(x')$  curve.  $x(t)$  is the position of the magnet relative to the PCB, and is moving in time. So, the whole sinusoid is moving back and forth along  $x'$ , but the  $d_1$  and  $d_2$  locations are stationary. With this understanding in place, we can substitute Eq. (6) into Eq. (4) and perform the integration, which results in the expressions in Eqs. (7) and (8) for  $\Phi$  and  $d\Phi/dt$ . These equations form the basis for efficient numerical simulation and guide the design process.

$$\Phi = \frac{-NIB_{\max} e^{-\alpha y(i)} p}{2\pi} \left\{ \left[ \sin \left( \frac{2\pi d_2}{p} \right) - \sin \left( \frac{2\pi d_1}{p} \right) \right] \sin \left( \frac{2\pi}{p} x(t) \right) + \left[ \cos \left( \frac{2\pi d_2}{p} \right) - \cos \left( \frac{2\pi d_1}{p} \right) \right] \cos \left( \frac{2\pi}{p} x(t) \right) \right\} \quad (7)$$

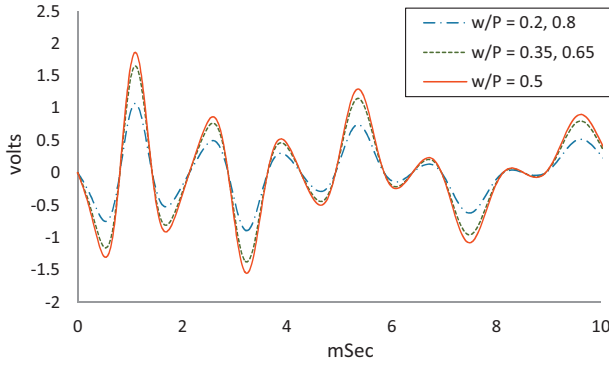


**Fig. 9.** Voltage contribution from each of three coils wired in series. Simulation performed for a suspended magnet displaced by 3 mm and released. Only the first few oscillations are shown.  $w/P$  is the coil width divided by the magnet pitch. The optimal value is 0.5.

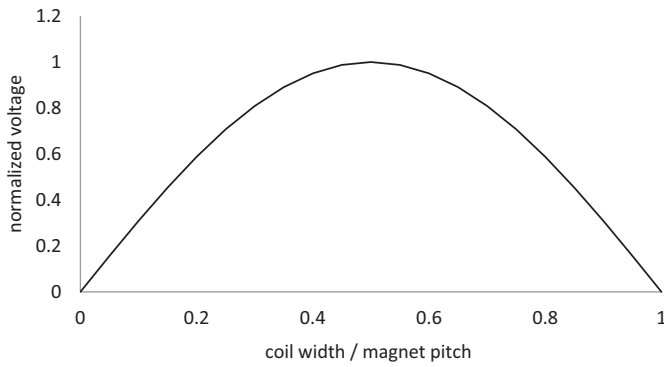


**Fig. 10.** Normalized voltage generated versus coil width to magnet pitch ratio.

$$\frac{d\Phi}{dt} - NlB_{\max} e^{-\alpha y(i)\dot{x}} \left\{ \left[ \sin\left(\frac{2\pi d_2}{p}\right) - \sin\left(\frac{2\pi d_1}{p}\right) \right] \cos\left(\frac{2\pi}{p}x(t)\right) - \left[ \cos\left(\frac{2\pi d_2}{p}\right) - \cos\left(\frac{2\pi d_1}{p}\right) \right] \sin\left(\frac{2\pi}{p}x(t)\right) \right\} \quad (8)$$

### 3.2. Effects of coil geometry

Referring back to Fig. 3, note that the width of the two coils on the top surface is different from one another. The width here refers not to the width of an individual metal trace, but to the distance between two parallel traces of a rectangular coil. Therefore,  $d_1$  and  $d_2$  in Eq. (8) are different for each coil and the voltage generated by each series coil must be calculated individually. The optimal coil has a width of one half the magnet pitch. However, it is possible for only one coil per layer of the PCB to have the optimal coil width. All other coils will be sub-optimal. There is, therefore a design tradeoff to be made in selecting the number of series coils in a layer. A larger number of coils corresponds to more voltage, but also more series resistance, which could hurt power production depending on the characteristics of the load. The wider or narrower a coil becomes with respect to one half the magnet pitch, the less productive it is in terms of energy generation, yet it contributes the almost exactly the same series resistance. Fig. 9 shows the voltage generated from each of five coils with different widths with respect to the magnet pitch (note: the voltages shown are for 6 layers of a PCB added together). Fig. 10 shows the normalized voltage generated by a coil vs. its width to pitch ratio. Note that no voltage is generated by a coil with the same width as the magnet pitch.

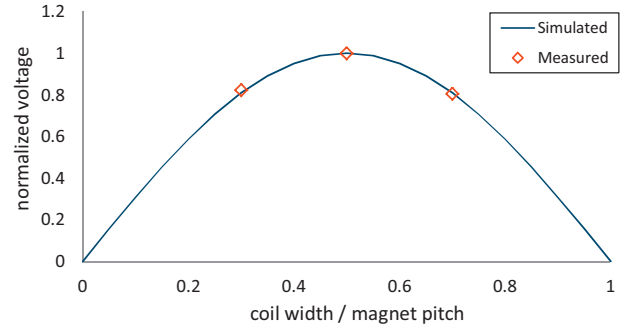


**Fig. 11.** Normalized voltage output versus coil width/magnet pitch ratio. Simulated and measured output shown. Measured data is the average of two measurements. The optimal ratio is 0.5.

The total flux captured by such a coil is always zero, and therefore there is no time rate of change in the magnetic flux and no voltage generated. Both Figs. 9 and 10 show open circuit voltage and highlight only the tradeoff between voltage generation and coil width. The same tradeoff will exist between power generation and coil width in the case of a real electrical load. Changing the coil width, while leaving the trace width and thickness the same, has virtually no effect on the series resistance of the coil. A coil that generates a higher open circuit voltage for the same series resistance will generate more power regardless of the impedance of the load.

There is another tradeoff to be made with regard to metal trace width and thickness when designing coils. A wider metal trace reduces series resistance, which is a source of loss, but allows space for fewer generating coils. Likewise a thicker metal trace reduces series resistance but requires a thicker PCB for the same number of layers. The model presented allows for easy optimization of coil geometry (coil width, trace width, trace thickness, and number of layers) for a given anticipated electrical load.

## 4. Results

Initially we built a bench top test setup to characterize and validate the model. After the model was validated, we used the model to design a series of prototype generators. The following sections will cover the results of the test bench setup and of one of the prototypes.

### 4.1. Test bench results

We used the bench top test setup to validate the effect of design parameters such as magnet to PCB spacing, coil width to magnet pitch ratio, input displacement, spring stiffness, etc. For example, Fig. 11 shows the simulated and measured normalized voltage versus coil width to magnet pitch ratio. The test setup was built with three different coil widths which were measured with a single multi-pole magnet. The experimental data matches the expected values very closely.

We measured the effect of the two different coil geometries shown in Fig. 3 and Fig. 5 with the test setup. The PCB that we built for the test setup has two sets of coils, one with the “standard” coil geometry shown in Fig. 3, and one with an alternate coil geometry shown in Fig. 5. We will call the coil configuration shown in Fig. 5 the alternate coil geometry as it was not the geometry used for final prototype designs. The coils are the same length and width and contain 2 series coils on a single layer of the PCB. Theoretically, the alternate coil geometry should produce 1.33 times more voltage than the standard geometry. Experimental data showed that the alternate coil geometry produced 1.5 times more voltage than the standard geometry. The alternate geometry also results in about



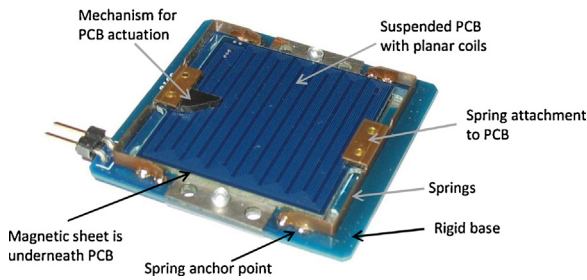


**Fig. 12.** Prototype generator. Size is approximately  $37 \times 37 \times 3$  mm. Magnet plate of size  $28 \times 30 \times 1$  mm is underneath the PCB. PCB is the proof mass.

10% higher coil resistance which reduces the power output somewhat. However, as the number of series coils per layer increases and the number of layers increases, the advantage of the alternate coil geometry decreases. This will be addressed in more detail in Section 5.

#### 4.2. Prototype results

Several prototypes have been built based on this technology, one of which is shown in Fig. 12. The PCB has 6 copper layers and is approximately 0.9 mm thick. In each layer of the PCB there are 5 coils wrapped in series in each of 7 loops. So the total number of coil loops is  $5 \times 7 \times 6 = 210$ . The copper lines are 0.6 mm wide and 0.072 mm thick (2 oz copper). This coil geometry was optimized for a  $20 \Omega$  load. The PCB is suspended over the top of the multi-pole magnet by means of two beryllium copper springs (see Fig. 12) (note that in this case, the PCB and magnet have been switched so that the PCB moves and the magnet is stationary). The designed gap between the magnet and PCB is 0.1 mm, although there is significant variation in this dimension from one prototype to the next due to manual assembly techniques. The resonant frequency of the device is 260 Hz.

The PCB and magnet were switched, such that the PCB is the oscillating proof mass, in order to increase the natural frequency, and therefore voltage generated. For a given force input, the velocity, and therefore the voltage generated, will be higher with a smaller proof mass. Note that the total energy generated will not go up, but the voltage will be higher, and the energy will be generated over a shorter period of time. This is illustrated in Fig. 13 which shows simulations of energy dissipated through a load resistor versus time for the device in Fig. 12 and an identical device in which the magnet is the proof mass. For both simulations the proof mass was displaced by 2 mm and released. The total mass of the PCB is 4 g and the total mass of the magnet is 10 g.

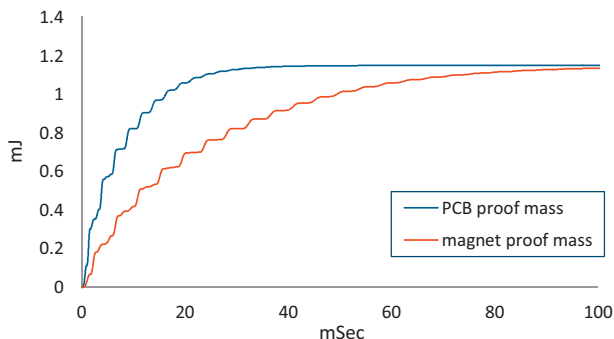


**Fig. 13.** Simulation results for a device with the PCB as the proof mass and a magnet as the proof mass. Graph shows energy dissipated through a matched resistor versus time. While both systems generate the same amount of energy, using the PCB as the proof mass generates energy faster and produces higher voltages.

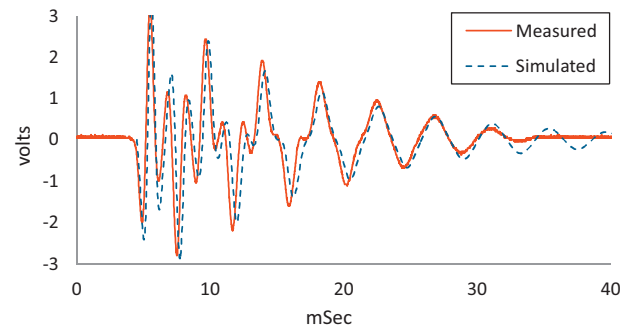


**Fig. 14.** Measured and simulated output voltage across a  $20 \Omega$  load resistor from an initial displacement of 2 mm.

The prototype shown in Fig. 12 is intended for direct force input. The proof mass is displaced with a force of 12 N, which results in a 2 mm displacement, and released. The voltage was measured across a  $20 \Omega$  resistor which matches the coil resistance. The measured and simulated voltage response is shown in Fig. 14. The generated energy is 1.1 mJ from 12 mJ of input energy resulting in an efficiency of 9%. The generator has also been used to charge a capacitor powering a wireless transmitter which can transmit 3 independent data packets from a single actuation cycle. The transmission current is approximately 25 mA. Fig. 15 shows the voltage across a  $60 \mu\text{F}$  storage capacitor and the combined current draw of the microprocessor and radio. The transceiver turns on at about 5 ms when the supply voltage is high enough for the transmitter IC to operate. The three data transmissions are clearly visible as the 25–30 mA pulses.

#### 5. Discussion

Note in Fig. 14 that there are two frequencies present in the voltage signal. The lower frequency is the mechanical oscillation of the proof mass. The higher frequency initially present in the signal results from the fact that the magnetic flux cutting the coils reverses faster than the mechanical motion reverses. This occurs because the initial mechanical displacement (2 mm) is the same as a single magnet pole, so there are two complete magnetic reversals (one full electrical cycle) in the first mechanical half-cycle. The higher initial frequency (double the mechanical frequency in this case) disappears as the proof mass displacement damps out and the mechanical oscillation is no longer large enough for two complete magnetic reversals in each mechanical half-cycle.

The alternate coil geometry shown in Fig. 5 can increase the voltage output as indicated in Section 4. This is true if there are relatively few series coils on a layer. For example, the PCB shown in Fig. 5 has only two series coils. However, the standard coil geometry shown in Fig. 3 can accommodate twice the number of series

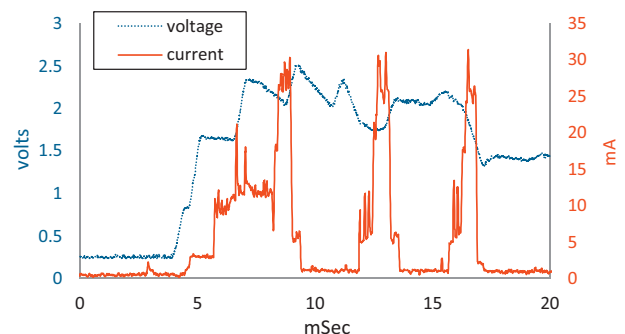


**Fig. 15.** Voltage across a  $60 \mu\text{F}$  storage capacitor and current draw demonstrating 3 data transmission packets for a single actuation.

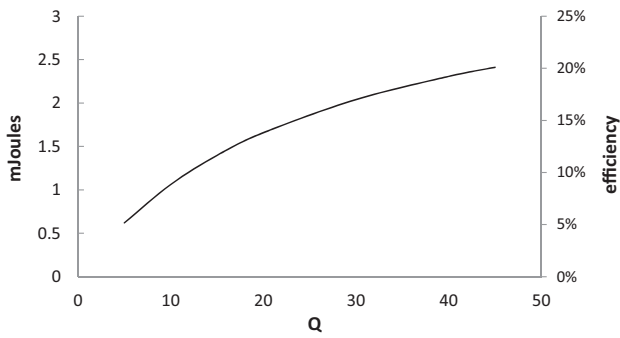


**Fig. 16.** Simulated output energy and efficiency for the prototype versus mechanical quality factor ( $Q$ ).

coils for a given coil pitch. While it is true that the outer and inner coils will be less efficient, in a practical system with practical constraints, we have found that the standard coil geometry performs better. For example, if the coils on the PCB shown in Fig. 12 were replaced with an optimal set of coils with the alternate geometry, the prototype would generate 1.0 mJ, or 9% less than the standard coils. Furthermore, there are other implementation issues with the alternate coil geometry. If this coil configuration were implemented on a 6 layer board the number of vias required would significantly reduce the capture area of the coils. Alternatively, blind vias could be used between each of the layers. This, however, would significantly increase board cost.

The mechanical damping ratio ( $\zeta$ ) for the device shown in Fig. 12 was measured to be 0.05 for a mechanical  $Q$  of 10 ( $b=0.59$  kg/s). The damping is primarily due to losses at the attachment points of the springs to the base which are soldered connections. The effective damping coefficient produced by the electromagnetic forces on the proof mass is 0.09 kg/s ( $Q=65$ ). So, most of the decay in oscillation is due to mechanical losses, not electromagnetic forces. The efficiency could be greatly improved by reducing the mechanical losses. Fig. 16 shows the potential output energy (and efficiency) to be gained by reducing the mechanical damping. A mechanical  $Q$  of 40 is not unreasonable if the soldered connections were replaced with more rigid mechanically clamped connections. Mechanical  $Q$ s far in excess of 40 have been reported in the literature for clamped connections [12]. The output efficiency could be increased by a factor of 2 simply by a reduction in the mechanical damping to achieve a  $Q$  of 40. While there is a significant increase in energy production, there is very little change in peak voltage. The increase in energy production comes from the fact that the proof mass oscillates for a longer time and therefore energy can be collected for a longer time. There is, however, a practical difficulty in capturing the energy at the end of the oscillation. From the perspective of the power electronics, it is much easier to capture the energy from the initial part of the ring-down when the voltage is high. As the oscillating voltage decreases, the power electronics need to produce a larger voltage gain in order to charge either a capacitor or battery. Without carefully designed power circuitry, the potential increase in efficiency by reducing the mechanical loss would not be achievable.

The power output is also very sensitive to the air gap between the PCB and magnets. In practice we tried to control this gap to 0.1 mm during assembly. Variation in this gap will result in a large variation in transducer performance. Fig. 17 shows the energy generated (and corresponding efficiency) versus the air gap. Note that the effect of reducing the air gap is to increase the electromagnetic forces and associated damping. The goal is for the majority of the kinetic energy to be “lost” to the transducer rather than to parasitic mechanical losses. More automated assembly methods could reduce this air gap to perhaps as little as 0.05 mm for a device the size of our prototype. In the ideal case, mechanical  $Q$  of

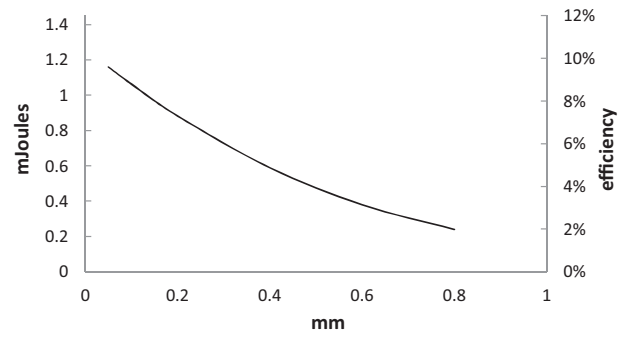


**Fig. 17.** Simulated energy and efficiency versus air gap between the magnet and PCB.

40 and a 0.05 mm air gap, the energy produced would be 2.4 mJ for an efficiency of 20%. It should be noted that reducing this air gap will also increase the mechanical damping due to viscous fluid flow. However, the damping coefficient due to viscous flow at a gap of 0.05 mm would only be approximately  $5.4 \times 10^{-4}$  kg/s, which is orders of magnitude lower than the damping due to the mechanical attachments.

The sensitivity to the air gap could be minimized by using a symmetric design with a magnet above and below the PCB. In this case the magnetic field is more uniform in the direction perpendicular to the magnet surface. However, two of the key objectives of the current work were to minimize device thickness and cost. The dual magnet configuration significantly increases both thickness and cost.

## 6. Conclusion

We have presented a planar linear energy harvesting transducer. The transducer can be used for devices that generate power from either a direct force input or from vibrations. We have demonstrated a generator powered by a direct force input. The generator employs novel manufacturing techniques to realize a thin multipole magnet and a novel coil configuration implemented in a multi-layer PCB. The measured results match theoretical models very closely resulting in a device efficiency of 9%. Further design enhancements could easily push the efficiency up to 20%. Finally, we have used the device to power a wireless system in which 3 data packets have been transmitted from a single actuation cycle.

## Acknowledgments

The authors would like to acknowledge the helpful input and design assistance of Dr. Brian Bircumshaw and Stewart Carl. This work was funded by the National Science Foundation under award 1127526.

## References

- [1] C.B. Williams, R.B. Yates, Analysis of a micro-electric generator for microsystems, in: *Transducers/Eurosensors*, 1995, pp. 369–372.
- [2] G. Lesieutre, G. Ottman, H. Hofmann, Damping as a result of piezoelectric energy harvesting, *Journal of Sound and Vibration* 269 (2004) 991–1001.
- [3] S. Roundy, P.K. Wright, J. Rabaey, A study of low level vibrations as a power source for wireless sensor nodes, *Computer Communications* 26 (2003) 1131–1144.
- [4] P.D. Mitcheson, T.C. Green, E.M. Yeatman, A.S. Holmes, Architectures for vibration-driven micropower generators, *Journal of Microelectromechanical Systems* 13 (2004) 1–12.
- [5] P.D. Mitcheson, E.M. Yeatman, G.K. Rao, A.S. Holmes, T.C. Green, Energy harvesting from human and machine motion for wireless electronic devices, *Proceedings of the IEEE* 96 (2008) 1457–1486.
- [6] C. Knight, J. Davidson, S. Behrens, Energy options for wireless sensor nodes, *Sensors* 8 (2008) 8037–8066.
- [7] Perpetuum Ltd., 2012.

- [8] Ferro Solutions, 2012.
- [9] EnOcean GmbH, 2012.
- [10] E. Lefeuvre, A. Badel, C. Richard, D. Guyomar, Piezoelectric energy harvesting device optimization by synchronous electric charge extraction, *Journal of Intelligent Material Systems and Structures* 16 (2005) 865–876.
- [11] S. Roundy, P.K. Wright, A piezoelectric vibration based generator for wireless electronics, *Smart Materials and Structures* 13 (2004) 1131–1142.
- [12] R. Torah, P. Glynn-Jones, M. Tudor, T. O'Donnell, S. Roy, S. Beeby, Self-powered autonomous wireless sensor node using vibration energy harvesting, *Measurement Science and Technology* 19 (2008) 125202.
- [13] Perpetuum Ltd., "PMG FSH Free Standing Harvester Datasheet," PMG FSH Technical Datasheet, May 2010.
- [14] D. Zhu, S. Beeby, J. Tudor, N. Harris, Vibration energy harvesting using the Halbach array, *Smart Materials and Structures* 21 (2012) 075020.
- [15] M. El-hami, P. Glynn-Jones, N.M. White, M. Hill, S. Beeby, E. James, et al., Design and fabrication of a new vibration-based electromechanical power generator, *Sensors and Actuators A: Physical* 92 (2001) 335–342.
- [16] H. Kulah, K. Najafi, An electromagnetic micro power generator, in: *Micro Electro Mechanical Systems*, IEEE International Conference, 2004, pp. 237–240.
- [17] S.P. Beeby, M.J. Tudor, N.M. White, Energy harvesting vibration sources for microsystems applications, *Measurement Science and Technology* 17 (2006) R175–R195.
- [18] D.P. Arnold, Review of microscale magnetic power generation, *IEEE Transactions on Magnetics* 43 (2007) 3940–3951.
- [19] a Z. Trimble, J.H. Lang, J. Pabon, A. Slocum, A device for harvesting energy from rotational vibrations, *Journal of Mechanical Design* 132 (2010) 091001.
- [20] P.C.-P. Chao, C.-T. Liao, L.D. Chao, P.C.-P. Chen, J.-T. Chen, W.-C. Hsu, W.-H. Chiu, C.-W. Lin, A miniaturized electromagnetic generator with planar coils and its energy harvest circuit, *IEEE Transactions on Magnetics* 45 (2009) 4621–4627.
- [21] S. Cheng, D.P. Arnold, A study of a multi-pole magnetic generator for low-frequency vibrational energy harvesting, *Journal of Micromechanics and Microengineering* 20 (2010) 025015.
- [22] S.H. Masato Sagaway, T. Mizoguchi, M. Asazuma, Method and system for producing sintered NdFeB magnet, and sintered NdFeB magnet produced by the production method, US Patent US 2012/0176212 A1 (2012).

## Biographies

**Shad Roundy** received his PhD in Mechanical Engineering from the University of California, Berkeley in 2003. From there he moved to the Australian National University where he was a senior lecturer for 2 years. After spending several years working in energy harvesting and MEMS related start-up companies, he joined the University of Utah as an Assistant Professor in 2012. Shad is the recipient of the DoE Integrated Manufacturing Fellowship, the Intel Noyce Fellowship, and was named by MIT's Technology Review as one of the world's top 100 young innovators for 2004. His research interests include energy harvesting and inertial sensing.

**Dr Eri Takahashi** is the founder and CEO of EcoHarvester, Inc. Dr. Takahashi has completed her Ph.D. in Applied Science and Technology at the University of California, Berkeley.